

Supporting Information

Directly catalytic synthesis of ultrasmall Cu₂O-coordinated carbon nitrides on ceria for multimodal antitumor therapy

Lijian Cao,^{§,a} Ziyang Feng,^{§,b} Ruiqian Guo,^b Qinyu Tian,^c Weiwen Wang,^b Xiao Rong,^b Mi Zhou,^b Chong Cheng,^{,b} Tian Ma,^{*,b} and Dawei Deng^{*,a}*

1. Materials

Cupric chloride dihydrate ($\text{CuCl}_2 \cdot \text{H}_2\text{O}$, 99.99%), cerium(III) chloride heptahydrate ($\text{CeCl}_3 \cdot 7\text{H}_2\text{O}$, 99.99%), hexamethylenetetramine (HMT, 99.0%), 3,3',5,5'-Tetramethylbenzidine (TMB, 99.0%), 5,5-dimethyl-1-pyrroline N-oxide (DMPO, 99%), potassium thiocyanate (KSCN, 99%), and dihydroethidium (HE, 95%) were purchased from Aladdin. Dicyanodiamide (DCD) was purchased from Keshi (Chengdu, China). Terephthalic acid (TA, 99%) was purchased from J&K Scientific. 9,10-diphenanthraquinone (DPA) was purchased from Thermo. 2,7-dichlorofluorescein diacetate (DCFH-DA) was purchased from Sigma. Tris (4,7-diphenyl-1,10-phenanthroline) ruthenium (II) dichloride ($\text{Ru}(\text{dpp})_3\text{Cl}_2$) was obtained from Maokang Biotechnology Co., Ltd. (Shanghai, China). Calcein acetoxymethyl (calcein-AM) and propidium iodide (PI) was purchased from Bestbio. CD31, CRT, and Ki-67 were purchased from Abcam; Annexin V-FITC Apoptosis Detection Kit was purchased from Beijing 4A Biotech Co., Ltd. Mitochondrial Membrane Potential Detection Kit (JC-1) was purchased from Solarbio. TUNEL was purchased from Promega.

2. Synthesis of $\text{Cu}_2\text{O}@\text{CeO}_2$ nanospheres

A one-step hydrothermal method was used to prepare $\text{Cu}_2\text{O}@\text{CeO}_2$ nanospheres. In a typical synthesis, different mole ratios of Cu/Ce (1:1, 1:2, and 1:3) were obtained by mixing $\text{CuCl}_2 \cdot \text{H}_2\text{O}$ and $\text{CeCl}_3 \cdot 7\text{H}_2\text{O}$ in 50 mL of deionized water followed by sonicating for 5 min, preserving the total amount of metal cations ($\text{Cu}^{2+} + \text{Ce}^{3+}$) as 1 mmol. Then the HMT aqueous solution (15 mmol HMT dissolved in 50 mL of deionized water followed by sonicating for 5 min) was added dropwise into the solution under vigorous magnetic stirring for 10 min. The mixture suspension was maintained at 75 °C in an oil bath for 4 h. The resulting product was isolated by centrifuging and washed with deionized water and ethyl alcohol three times and followed by drying in an oven at 60 °C overnight.

3. Synthesis of $\text{Cu}_2\text{O}-\text{CN}_x@\text{CeO}_2$ nanospheres

In a normal procedure, the as-prepared $\text{Cu}_2\text{O}@\text{CeO}_2$ (20 mg) powder was placed at one end of the porcelain boat, and the DCD granule (160 mg) was placed at another end of the porcelain boat. Then, the porcelain boat was covered, transferred to an argon oven, heated to 400 °C with a ramp rate of 5 °C min^{-1} , and held for 2 h. The resulting product was isolated by centrifuging and washed with deionized water and ethyl alcohol three times together with sonicating to remove surface-adsorbed ammonia and followed by drying in an oven at 60 °C overnight to yield $\text{Cu}_2\text{O}-\text{CN}_x@\text{CeO}_2$ nanospheres. In order to study the influence of the structure, morphology, and performance of different pyrolysis temperatures. The same precursors were conducted at 300, 500, and 600 °C.

4. Characterizations

The crystal structure of all the products was confirmed by powder XRD using a Rigaku Ultima IV with Cu K α irradiation. Diffraction patterns were collected at a scan rate 2° min⁻¹ at 0.02° steps from 20° to 80°. The surface morphologies, sizes, and elemental compositions of catalysts were analyzed by scanning electron microscope (SEM) and high-resolution transmission electron microscope (HR-TEM, Tecnai G2 F20 S-TWIN) embedded with energy-dispersive X-ray spectroscopy (EDX). For aberration-corrected scanning transmission electron microscopy (AC-STEM) analysis, STEM investigations were performed on FEI Titan Themis 60-300 at 200 kV. The surface elemental composition and all binding energies were measured by X-ray photoelectron spectroscopy (XPS, ESCAL 250) with Al K α monochromatic X-ray sources. Fourier transform infrared (FTIR) spectra were recorded on a Nicolet-Is50 FTIR spectrometer using the KBr pellet technique. Electron paramagnetic resonance (EPR) measurements were carried out via the Bruker EPR EMX Plus (Bruker Ltd, USA) at a frequency of 9.8 GHz (microwave power: 1 mW). Inductively coupled plasma mass spectrometry (ICP-MS) was recorded on Thermo Scientific iCAP RQ.

5. Peroxidase (POD)-like catalytic assays

24 μ L TMB (10 mg mL⁻¹) was added into 2 mL PBS (pH = 4.5) containing a reaction system of Cu₂O-CN_x@CeO₂ (25 μ g mL⁻¹) and H₂O₂ (1.25 mM), followed by the analysis using UV-vis spectrophotometer. US irradiation (1 MHz, 1 W cm⁻², 30% duty cycle) was used during the measurement process to explore US-enhanced POD-like activity.

6. POD-like dynamic parameters

Meanwhile, the kinetic study of Cu₂O-CN_x@CeO₂ using H₂O₂ as substrate (0.625, 1.250, 2.500, 3.750, 5.000, 6.250, 7.500 mM) was performed at a fixed concentration of Cu₂O-CN_x@CeO₂ (12.5 μ g mL⁻¹). All reactions were monitored by measuring the absorbance after different reaction times, and the Michaelis-Menten constant was calculated based on the Michaelis-Menten saturation curve. For each H₂O₂ concentration, the initial reaction rates (V_0) of the generation of ROS were calculated from the absorbance variation using the Beer-Lambert Law (Equation (1)) (with an ϵ of 39 000 M⁻¹ cm⁻¹ for oxTMB). The reaction rates were then plotted against their corresponding H₂O₂ concentration and then fitted with the Michaelis–Menten curves (Equation (2)). Furthermore, a linear double-reciprocal plot (Lineweaver–Burk plot, Equation (3)) was used to determine the maximum velocity (V_{max}) and Michaelis–Menten constant (K_m). Furthermore, the turnover number (TON) was calculated according

to equation (4). The same as H₂O₂, the kinetic study was performed through changing the concentration of TMB (0.1, 0.2, 0.4, 0.5, 1.0, 2.0, 1.5 mM).

$$A = \varepsilon lc \quad (1)$$

$$V_0 = \frac{V_{\max} \times [S]}{K_m + [S]} \quad (2)$$

$$\frac{1}{V_0} = \frac{K_m}{V_{\max}} \times \frac{1}{[S]} + \frac{1}{V_{\max}} \quad (3)$$

$$\text{TON} = V_{\max}/[E_0] \quad (4)$$

[S] is the concentration of H₂O₂ or TMB, and [E₀] is the molar concentration of active center metal in biocatalyst.

7. Catalase (CAT)-like activity assays

The O₂ generation was detected by Dissolved Oxygen Meters. 20 μL of Cu₂O-CN_x@CeO₂ (final concentrations: 10 μg mL⁻¹) and 200 μL of H₂O₂ (final concentration: 0.1 M) were added into 20 mL PBS (pH=5.8), respectively. The O₂ concentration was recorded at different time points.

8. Detection of superoxide radical

The generation of •O₂⁻ was evaluated by an EPR spectrometer and trapped by DMPO/DMSO. 50 μL of catalysts (1 mg mL⁻¹, DMSO), 20 μL of H₂O₂ (0.1 M), and 10 μL DMPO were added into 500 μL DMSO and mixed for 1 min; after generating free radical, the characteristic peak signals detected by an EPR spectrometer. Also, the generation of •O₂⁻ was further confirmed by an •O₂⁻ specific probe hydroethidine (HE). 10 μL Cu₂O-CN_x@CeO₂ (2 mg mL⁻¹) was mixed with 40 μL HE (1 μg mL⁻¹) and 10 μL H₂O₂ (0.1 M) in 1 mL PBS (pH=4.5), after ultrasound irradiation (1 MHz, 1 W cm⁻², 30% duty cycle) followed by the analysis using a fluorescence microplate reader.

9. Detection of singlet oxygen

The generation of •OH was also evaluated by an EPR spectrometer and trapped by DMPO. 50 μL of catalysts (1 mg mL⁻¹, DMSO), 20 μL of H₂O₂ (0.1 M), and 10 μL DMPO were added into 500 μL PBS (pH=4.5) and mixed for 1 min after generating free radical, the characteristic peak signals detected by an EPR spectrometer. Also, the generation of •OH was further confirmed by an •OH-specific

terephthalic acid (TA). 1 mL $\text{Cu}_2\text{O-CN}_x@\text{CeO}_2$ (2 mg mL^{-1}) was mixed with 10 mL TA (2.25 mg mL^{-1}) in 9 mL DI water and stirring in the dark for 30 min, after light irradiation (14 A) followed by the analysis using a fluorescence microplate reader.

10. Detection of singlet oxygen

As for $^1\text{O}_2$ detection, $\text{Cu}_2\text{O-CN}_x@\text{CeO}_2$ ($50 \text{ }\mu\text{g mL}^{-1}$) was mixed with DPA ($1 \text{ }\mu\text{g mL}^{-1}$) at a volume ratio of 1:40, followed by the analysis using a UV-vis spectrophotometer. The decomposition rate of DPA by $\text{Cu}_2\text{O-CN}_x@\text{CeO}_2$ was recorded after light irradiation (14 A), and the relative absorbance changes of DPA at 378 nm were used to quantify the decomposition rate.

11. In vitro cytotoxicity

Human Umbilical Vein Endothelial cells (HUVECs) were incubated for 24 h in a 96-well plate, each well containing 1×10^5 cells. The medium of the 96-well plate was discarded and then washed with phosphate-buffered saline. Subsequently, a complete medium containing $\text{Cu}_2\text{O-CN}_x@\text{CeO}_2$ at a serial concentration of 5, 10, 30, and $40 \text{ }\mu\text{g mL}^{-1}$ was added to a 96-well plate, followed by incubation for 24 h. Cell Counting Kit-8 (CCK8) assay was performed according to a standard protocol to determine cell viability.

12. Cell culture and internalization

B16F10 melanoma cells obtained from ATCC (American Type Culture Collection) were cultured in RPMI medium supplemented with 10% fetal bovine serum, 100 IU mL^{-1} penicillin and $100 \text{ }\mu\text{g mL}^{-1}$ streptomycin in a humidified incubator (37°C , 5% CO_2 , 21% O_2). Cell internalization of $\text{Cu}_2\text{O-CN}_x@\text{CeO}_2$ was estimated by transmission electron microscopy (TEM). $\text{Cu}_2\text{O-CN}_x@\text{CeO}_2$ ($40 \text{ }\mu\text{g mL}^{-1}$) were incubated with B16F10 cells over 12h. Cells were washed by PBS and fixed in 4% paraformaldehyde, before observed in TEM.

13. Fluorescence imaging of live/dead cells.

For fluorescence imaging, B16F10 cells were incubated with $\text{Cu}_2\text{O-CN}_x@\text{CeO}_2$ ($40 \text{ }\mu\text{g mL}^{-1}$) for 12 h, followed by US irradiation (1 MHz , 1 W cm^{-2} , 30% duty cycle) for 60 s and Laser excitation (14 A) for 180 s. The treated cells were stained with calcein-AM (AM, live cell, green color) and propidium iodide (PI, dead cell, red color) following the protocol.

14. Flow cytometry for cell apoptosis analysis

B16F10 cells were seeded in 12-well plates and allowed to adhere overnight. The culture media were then replaced by $\text{Cu}_2\text{O-CN}_x@\text{CeO}_2$ ($40 \mu\text{g mL}^{-1}$) in RPMI 1640 and incubated for another 12 h. After co-incubation, the cells were collected by centrifugation. Then, the Annexin V-FITC/PI Apoptosis Detection Kit (Beijing 4A Biotech Co., Ltd) was used to stain the cells before the flow cytometry analysis. According to the fluorescence intensity, cell populations are assigned into four quadrants, including live, early apoptotic, late apoptotic, and necrotic cells.

15. Detection of intracellular ROS production

DCFH-DA was used to detect the intracellular ROS generation ability of the $\text{Cu}_2\text{O-CN}_x@\text{CeO}_2$ nanoagent. B16F10 cells were seeded onto 24-well plates overnight, and then, $\text{Cu}_2\text{O-CN}_x@\text{CeO}_2$ ($40 \mu\text{g mL}^{-1}$) was added to each well and incubated for 8 h at 37°C . Subsequently, DCFH-DA was used as a ROS fluorescence probe by incubating it for 30 min. After washing with PBS, the intracellular fluorescence was monitored using an Olympus IX 83 instrument and flow cytometry.

16. HIF-1 α Immunostaining

HIF-1 α immunostaining was carried out in B16F10 cells incubated in acid media with $\text{Cu}_2\text{O-CN}_x@\text{CeO}_2$ (20 or $40 \mu\text{g mL}^{-1}$) under hypoxic condition. Hypoxic condition was achieved by incubation in hypoxia chamber containing 1% O_2 , 5% CO_2 , and 94% N_2 gas for 24 h. B16F10 cells treated without or with $\text{Cu}_2\text{O-CN}_x@\text{CeO}_2$ in different concentration (20 and $40 \mu\text{g mL}^{-1}$) were incubated in acid media under hypoxic conditions for 24 h, followed by staining with primary antibody against HIF-1 α (1:500, Abcam, ab179483) and Alexa Fluor 488-labeled secondary antibody (1:200, Abcam, ab150077). F-actin was co-stained using rhodamine phalloidin (1:200, Solarbio).

17. O_2 detection

The detection of intracellular O_2 was observed by $\text{Ru}(\text{BPy})_3\text{Cl}_2$. The cells were cultured first under hypoxic conditions for 24h, then incubated without or with $\text{Cu}_2\text{O-CN}_x@\text{CeO}_2$ in different concentration (20 and $40 \mu\text{g mL}^{-1}$). The cells were stained with $\text{Ru}(\text{BPy})_3\text{Cl}_2$ to detect O_2 subsequently.

18. JC-1 staining

Like AM/PI staining, the treated cells were stained with a JC-1 working solution for 20 min. The cells were washed with PBS three times and incubated in Hoechst for 10 min. The cells were washed with PBS three times and observed using a CLSM.

19. Tumor model

Balb/c mice were purchased from Beijing Huafukang Biotechnology Co., Ltd. To form the animal melanoma model, 100 μ L of logarithmically growing B16F10 cells (about 1×10^6 cells) were injected into the subcutaneous layer of the forelimb near the back with a fine needle to form a homogeneous dermatocollus. The Sichuan University Animal Ethics Committee has approved all the experimental protocols. And the assigned approval number is 20220621003.

20. In vivo therapeutic effects

Mice with tumors were randomized into six groups, each $n=4$, on 6 to 8 week old male Balb/c mice. Insert needle very superficially to inject cells, soon after preparation. Observe mice for tumor growth and estimate tumor scale. When the tumor volume reached 150~200 mm^3 , tumor treatment in the suit was carried out. The mice were divided into 6 groups according to the different treatment methods: (1) Control group: PBS group, (2) PBS + US + L group, (3) $\text{Cu}_2\text{O-CN}_x@\text{CeO}_2$, (4) $\text{Cu}_2\text{O-CN}_x@\text{CeO}_2$ + US, (5) $\text{Cu}_2\text{O-CN}_x@\text{CeO}_2$ + L, (6) $\text{Cu}_2\text{O-CN}_x@\text{CeO}_2$ + US + L, and each group had four mice. The ultrasonic condition was kept at intensity (2.5 W cm^{-2}), frequency (1 MHz), duty cycle (30%), time (5 min), and Laser condition was conducted at the intensity of 14 A, duration time of 5 min. Mice were injected with $\text{Cu}_2\text{O-CN}_x@\text{CeO}_2$ nanoagents (10 mg kg^{-1}), and the treatment with ultrasound and laser was conducted after 4 h intra-tumoral treatment, which was repeated every three days. The weight of tumor-bearing mice was measured at a fixed time point, and the curve of weight change with time was drawn. The long and short axis of the tumor were measured with a vernier caliper, the tumor volume was calculated by the formula: $\text{volume} = \text{length} \times \text{width}^2/2$, the curve of relative tumor volume change was drawn, the tumor growth inhibition (TGI) was calculated by the formula: $\text{TGI} = (\text{Tumor volume in the control group} - \text{tumor volume in experiment group})/\text{Tumor volume in control group} \times 100\%$ For H&E, CD31, Tunnel, CRT, Ki 67 staining, tumors with various treatments were collected after execution.

To check metastatic melanoma, cells were injected both beneath skin and through caudal veins. When the tumor volume reached 150~200 mm^3 , tumor treatment in the suit was carried out. The mice were divided into 2 groups according to the different treatment methods: (1) Control group: PBS group, (2) $\text{Cu}_2\text{O-CN}_x@\text{CeO}_2$ + US + L group. The ultrasonic condition was kept at intensity (2.5 W cm^{-2}),

frequency (1 MHz), duty cycle (30%), time (5 min), and Laser condition was conducted at the intensity of 14 A, duration time of 5 min. Mice of group 2 were injected with $\text{Cu}_2\text{O-CN}_x\text{@CeO}_2$ nanoagents (10 mg kg^{-1}), and the treatment with ultrasound and laser was conducted after 4 h intra-tumoral treatment, which was repeated every three days. The metastatic melanoma of lungs was evaluated.

21. Statistical analysis

Statistical analyses were performed using GraphPad Prism 8.0 software (GraphPad Software Inc.). All data are expressed as the mean \pm SD. Statistical significance was assessed by one-way analysis of variance compared to the control groups. Differences were considered significant at $P < 0.05$.

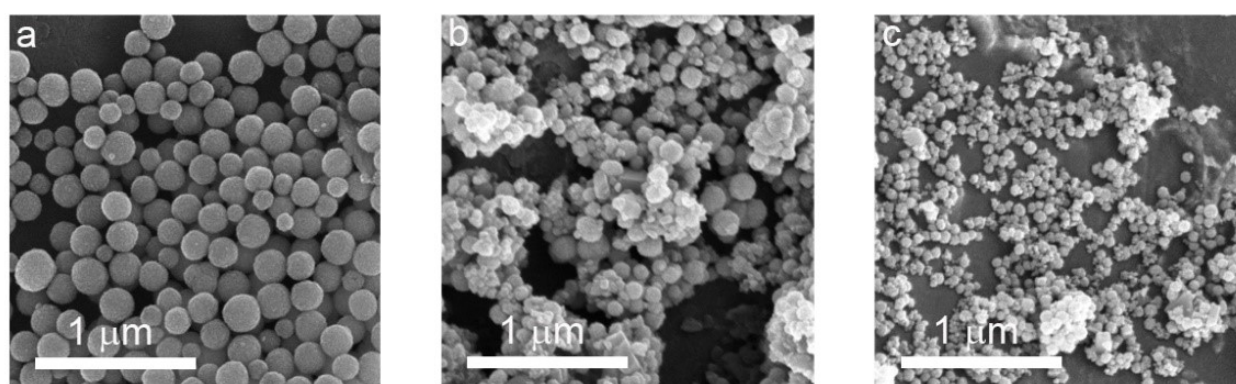


Figure S1. SEM images of $\text{Cu}_2\text{O@CeO}_2$ synthesized with different mole ratios of Cu:Ce, (a) 1:1, (b) 1:2, (c) 1:3.

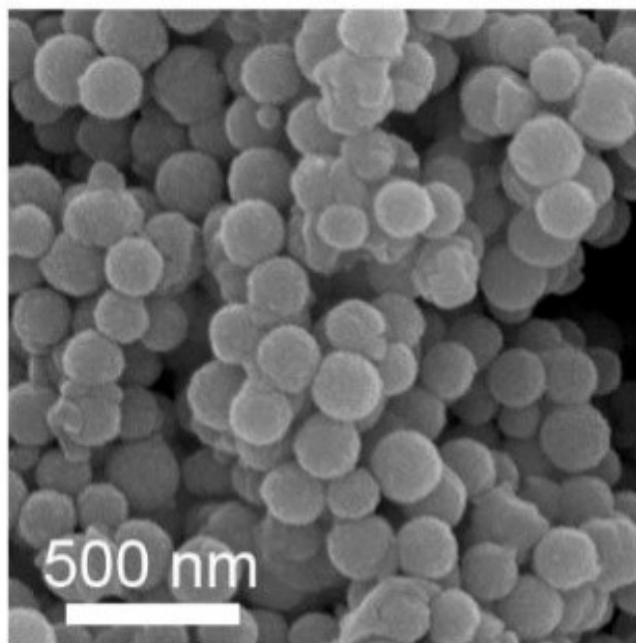


Figure S2. SEM images of $\text{Cu}_2\text{O}@\text{CeO}_2$ pyrolyzed with DCD at 300°C .

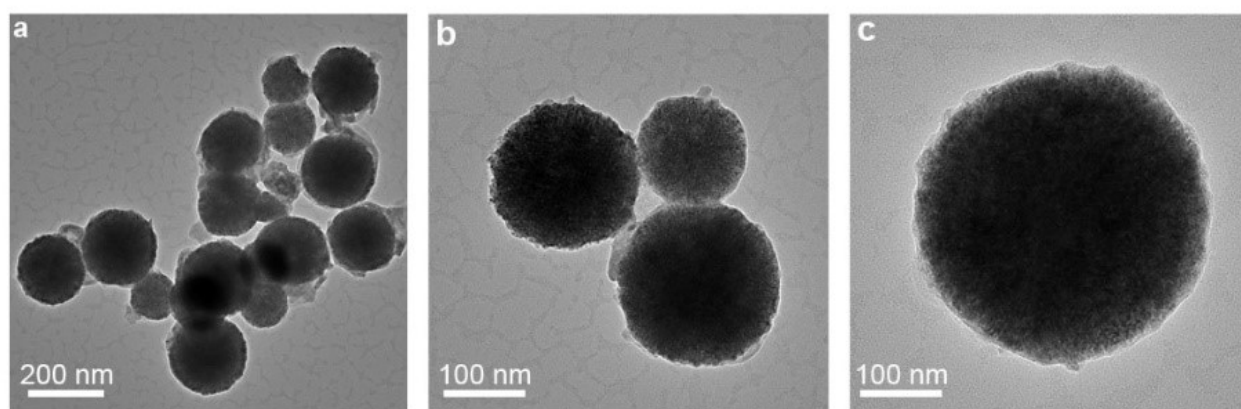


Figure S3. TEM images of $\text{Cu}_2\text{O}-\text{CN}_x@\text{CeO}_2$.

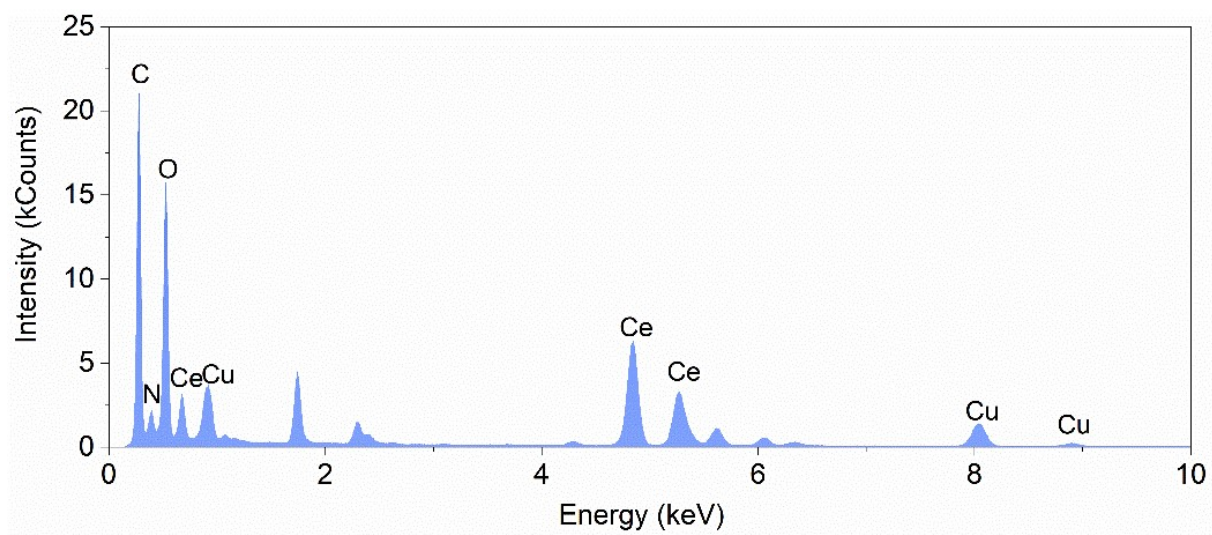


Figure S4. EDX of $\text{Cu}_2\text{O-CN}_x@\text{CeO}_2$.

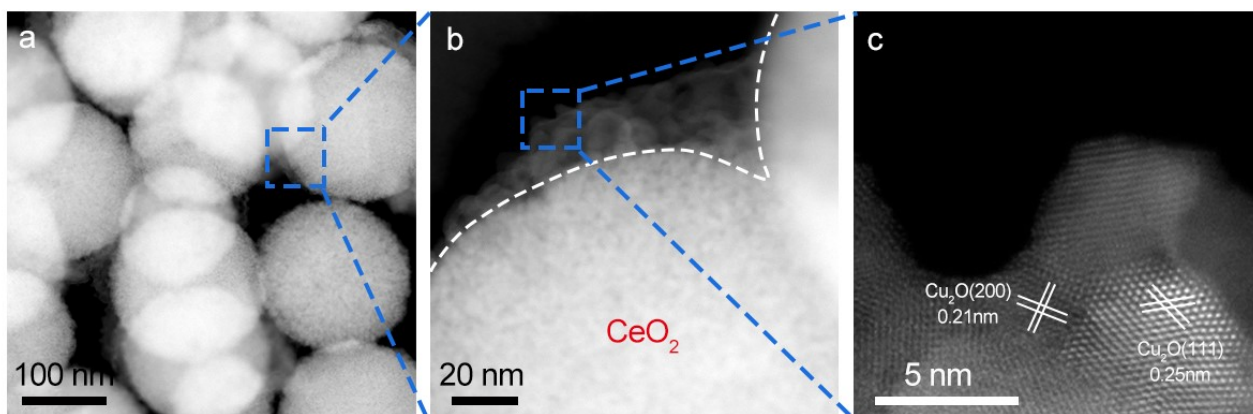


Figure S5. (a)-(c) HAADF-STEM images of $\text{Cu}_2\text{O-CN}_x@\text{CeO}_2$.

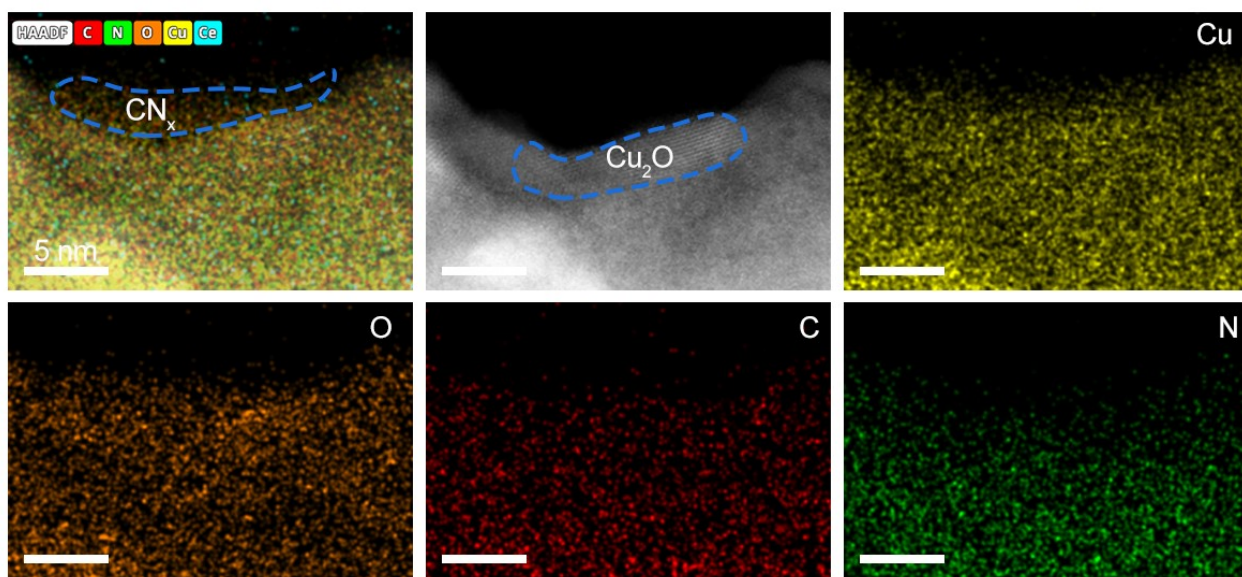


Figure S6. HAADF-STEM image of Cu_2O particles on carbon nitrides substrate and corresponding atomic-resolution EDX elemental mapping.

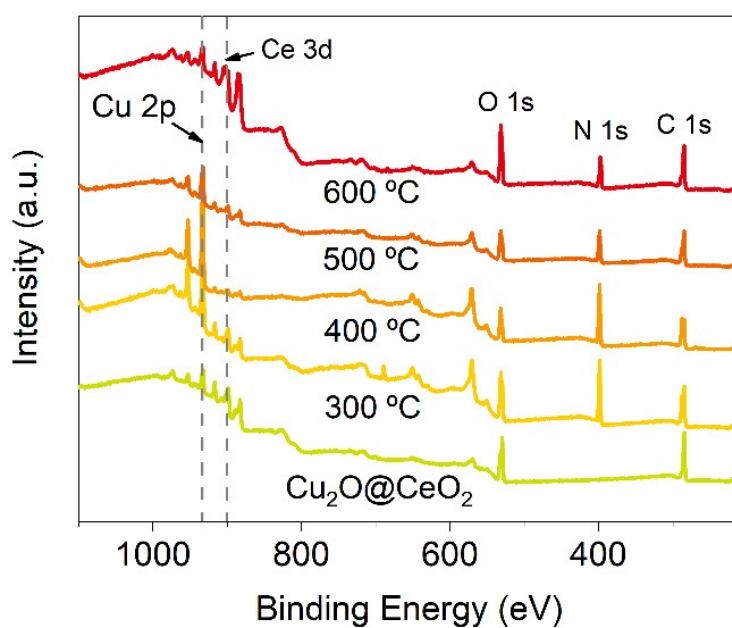


Figure S7. XPS survey scanning of $Cu_2O@CeO_2$ and corresponding samples obtained from different temperatures.

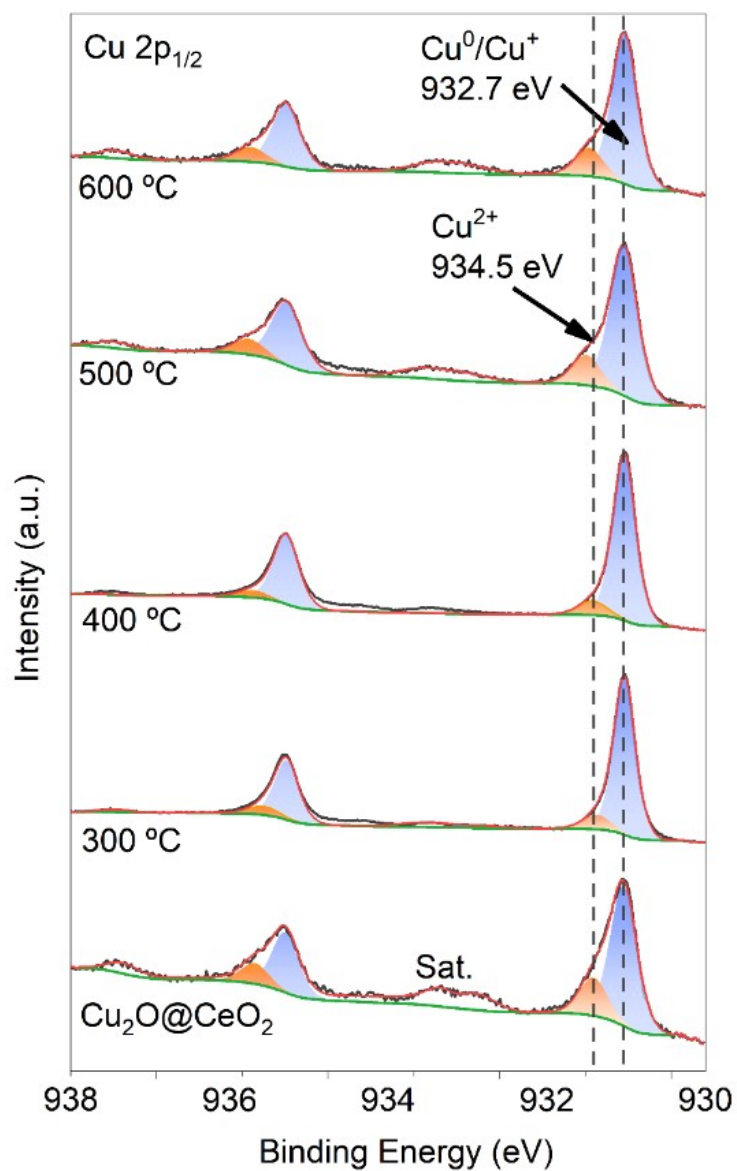


Figure S8. High-resolution Cu 2p XPS spectra of Cu₂O@CeO₂ and corresponding samples obtained from different temperatures.

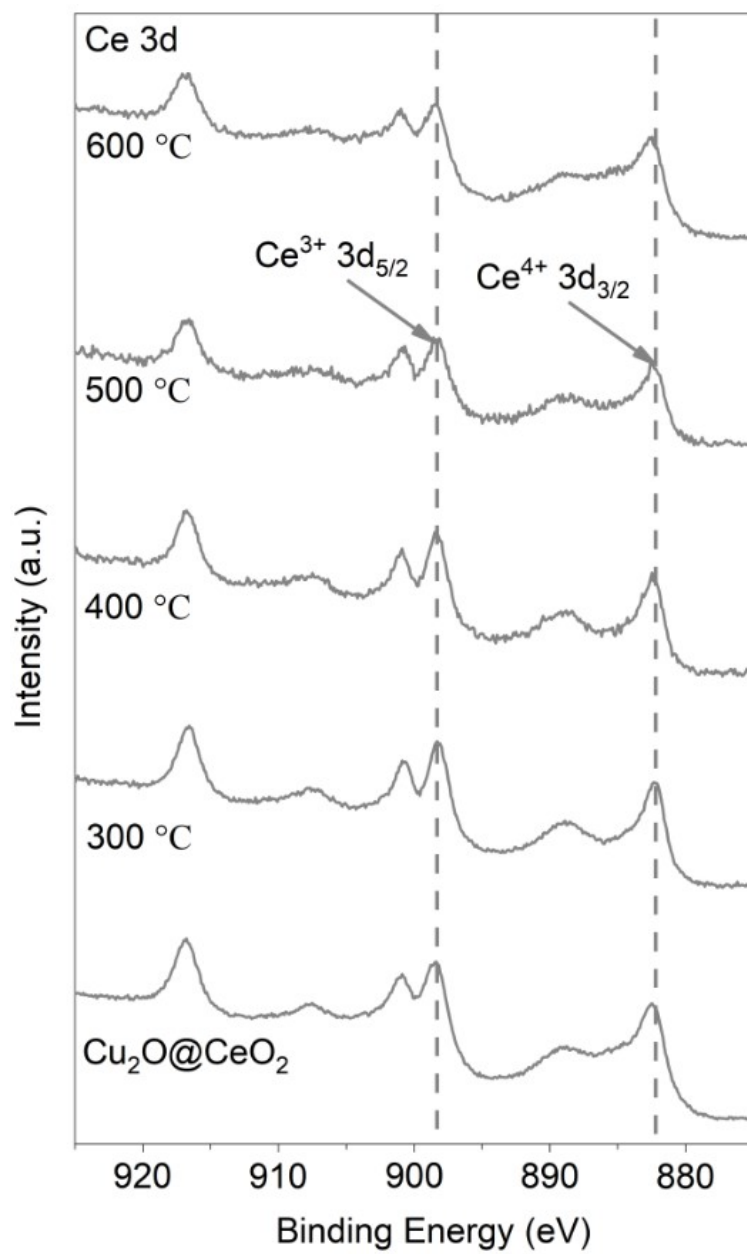


Figure S9. High-resolution Ce 3d XPS spectra of Cu₂O@CeO₂ and corresponding samples obtained from different temperatures.

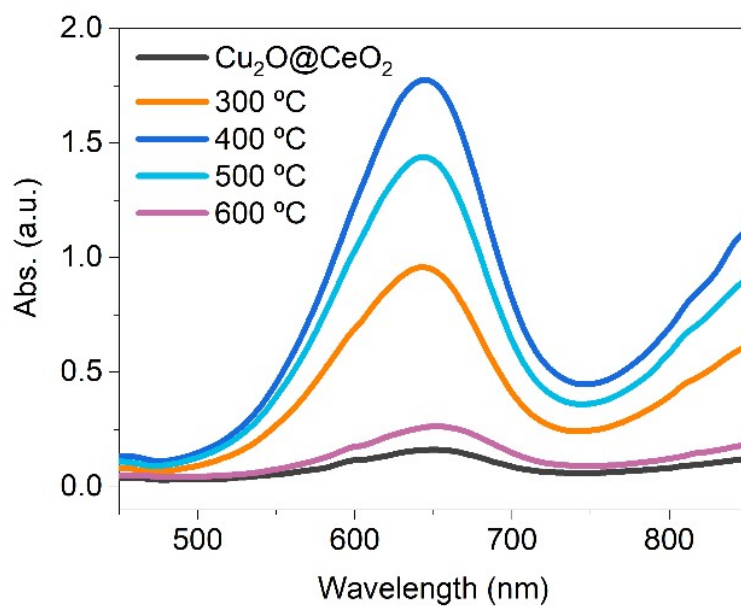


Figure S10. (a) POD-like properties of $\text{Cu}_2\text{O}@ \text{CeO}_2$ and corresponding samples obtained from different temperatures.

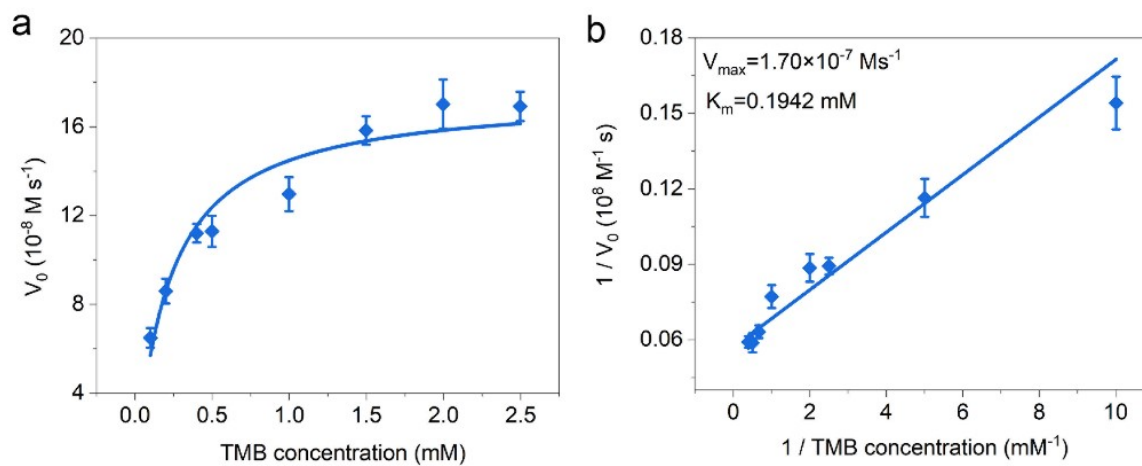


Figure S11. (a) Michaelis–Menten kinetic analysis and (b) Lineweaver–Burk plotting for $\text{Cu}_2\text{O}-\text{CN}_x@ \text{CeO}_2$ with TMB as substrate.

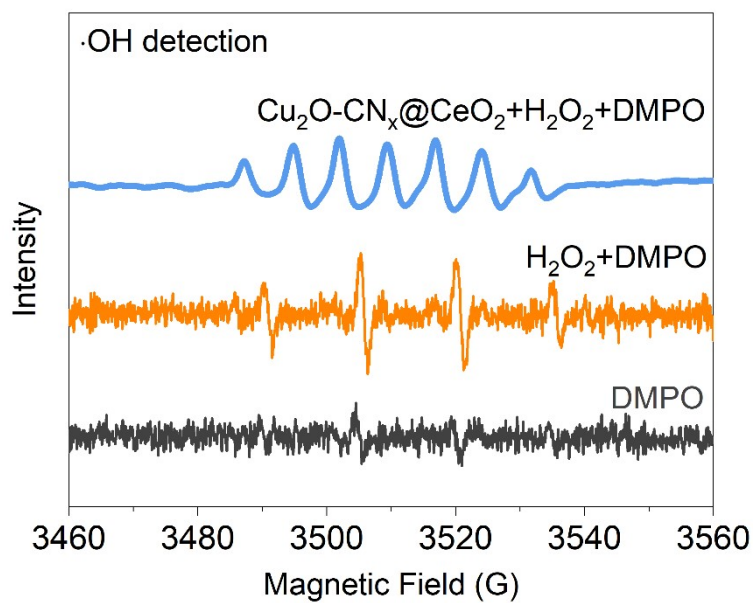


Figure S12. EPR spectra for the detection of $\cdot\text{OH}$ generated from different systems.

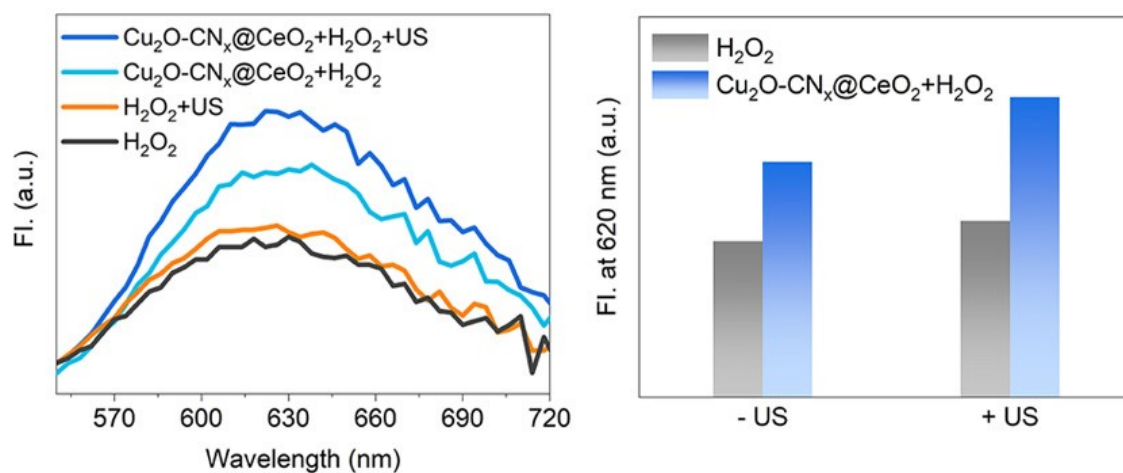


Figure S13. (a) Fluorescence spectrum and (b) fluorescence intensity at 620 nm of HE with or without ultrasound irradiation.

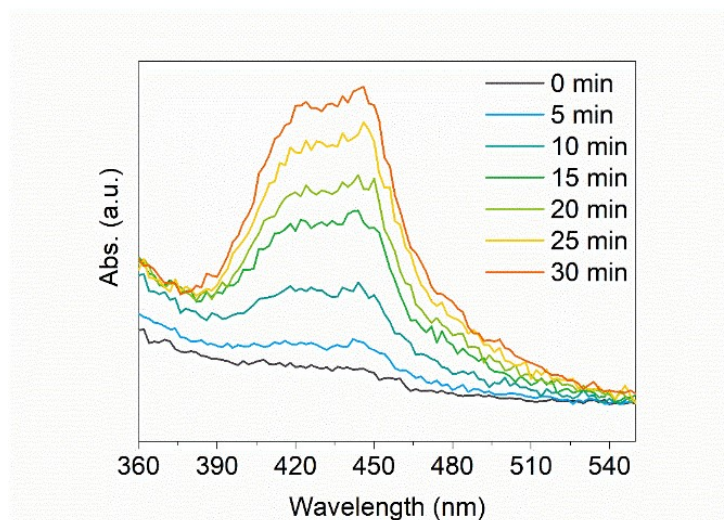


Figure S14. Time-dependent TA fluorescence spectrum of $\text{Cu}_2\text{O-CN}_x@\text{CeO}_2$ with light irradiation.

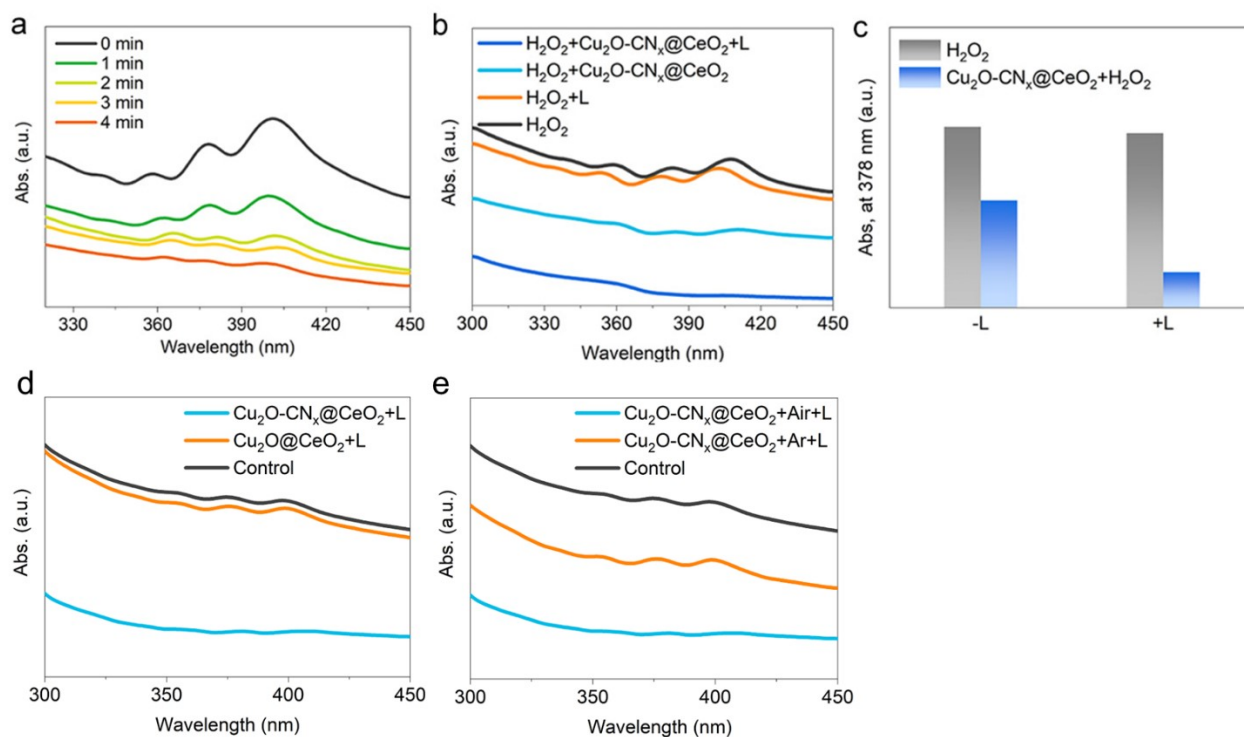


Figure S15. (a) Time-dependent catalytic oxidation of DPA by $\text{Cu}_2\text{O-CN}_x@\text{CeO}_2$ with light irradiation. (b) UV-vis absorption spectra and (c) absorbance values at 378 nm of DPA with or without light irradiation. (d) Comparison of catalytic oxidation of DPA by $\text{Cu}_2\text{O}@\text{CeO}_2$ and $\text{Cu}_2\text{O-CN}_x@\text{CeO}_2$ with light irradiation. (e) Comparison of catalytic oxidation of DPA by $\text{Cu}_2\text{O-CN}_x@\text{CeO}_2$ with and without light irradiation.

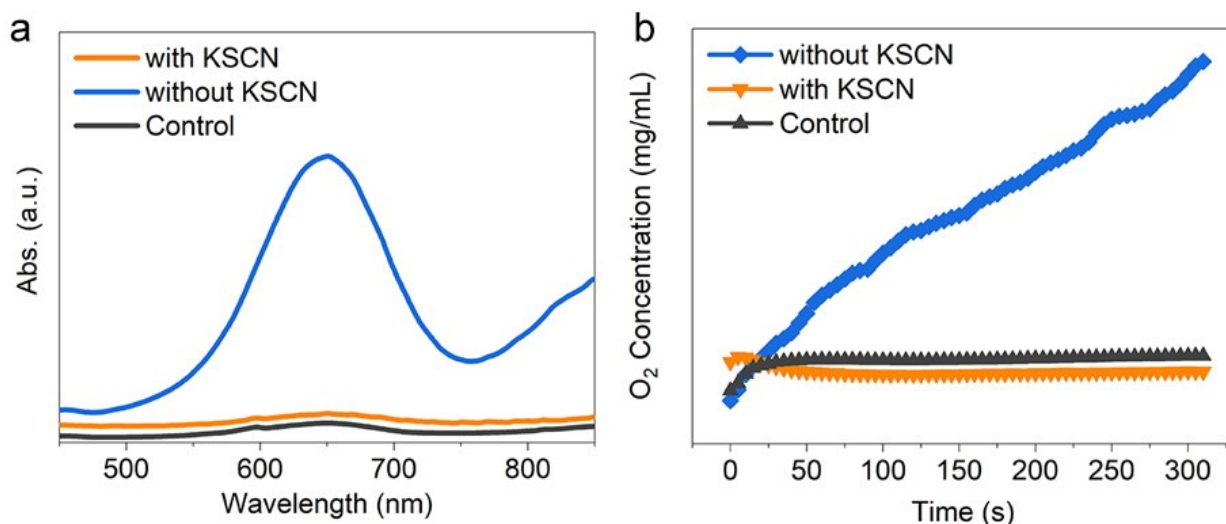


Figure S16. a) POD-like and b) CAT-like catalyst poisoning experiment for $\text{Cu}_2\text{O-CN}_x@\text{CeO}_2$ with KSCN.

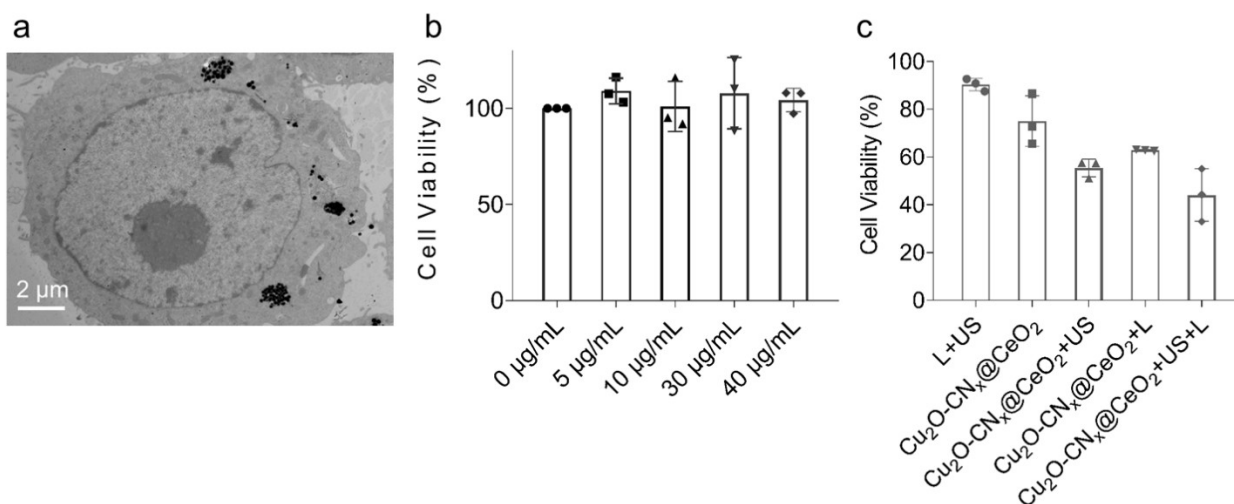


Figure S17. (a) TEM image of $\text{Cu}_2\text{O-CN}_x@\text{CeO}_2$ treated B16F10 cells. (b) HUVEC viability after incubated with $\text{Cu}_2\text{O-CN}_x@\text{CeO}_2$ for 24 h at different concentrations. (c) HUVEC viability after different treatments for 24 h.

As shown in Figure S17a, TEM image observed the $\text{Cu}_2\text{O-CN}_x@\text{CeO}_2$ in cells incubated, confirming the cell internalization. As shown in Figure 17c, due to the photodynamic effect of the material itself and the presence of oxygen in the normal tissue, it will cause certain killing to the normal cells.

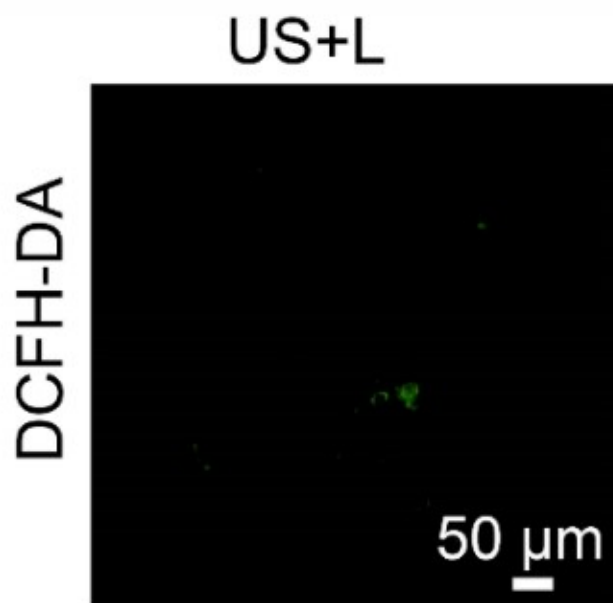


Figure S18. Fluorescence images of DCFH-DA stained B16F10 cells after US + L treatment.

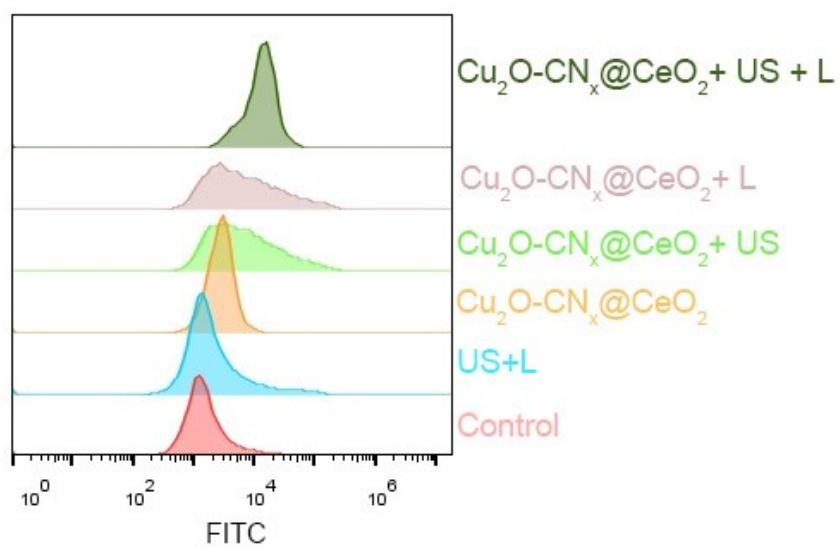


Figure S19. Detection of ROS level after different treatments by flow cytometry.

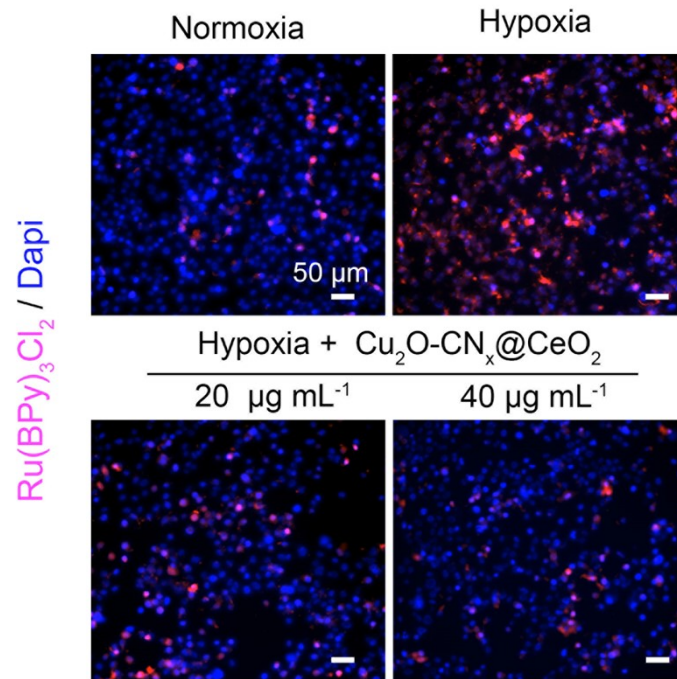


Figure S20. Cu₂O-CN_x@CeO₂ increased the intracellular oxygenation as examined using the oxygen indicator Ru(BPy)₃Cl₂.

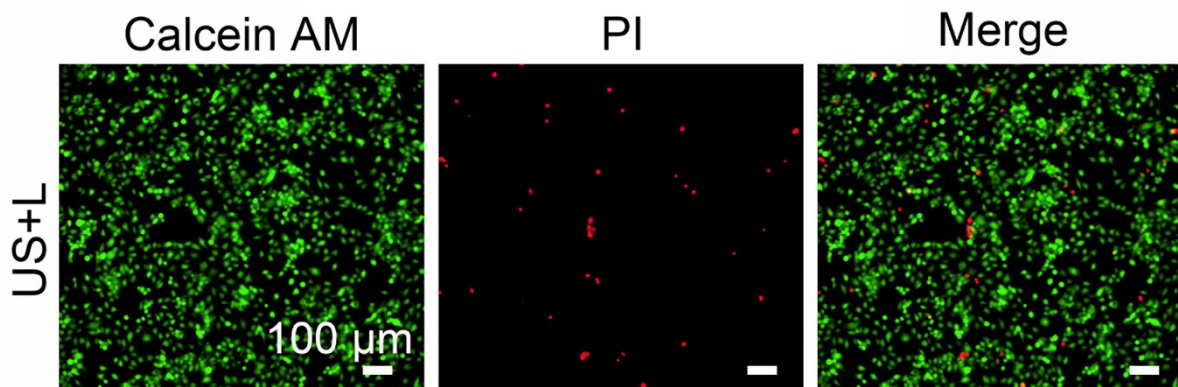


Figure S21. Fluorescence images of calcein-AM/PI stained B16F10 cells after US + L.

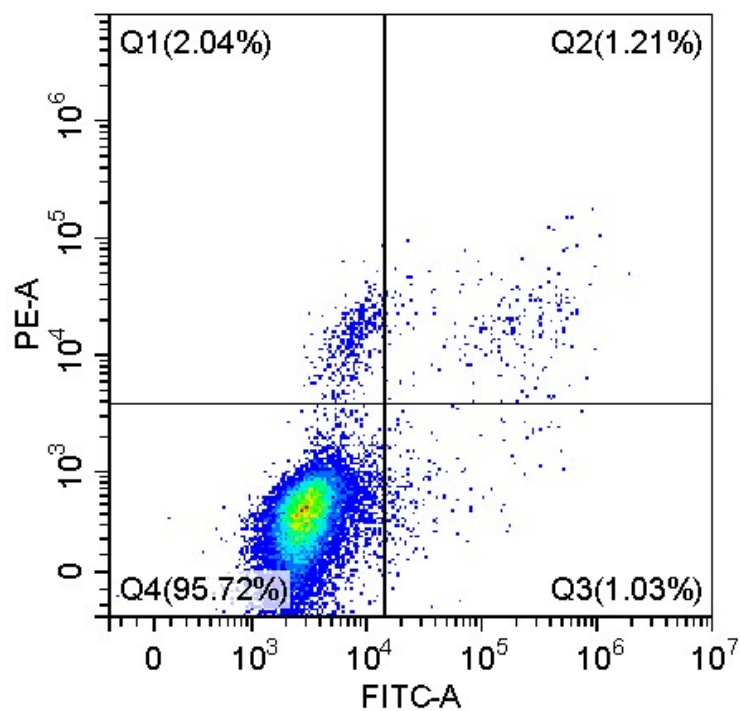


Figure S22. Fluorescein–annexin V-FITC and PI staining assay of B16F10 cells after US + L.

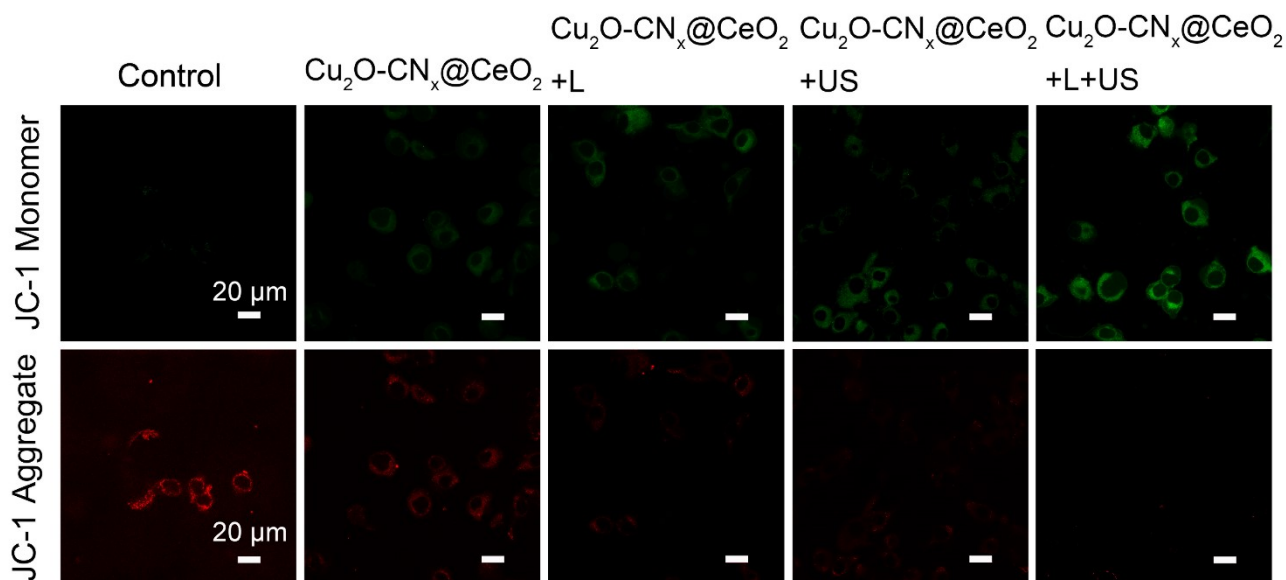


Figure S23. Mitochondrial membrane potential ($\Delta\psi_m$) in B16F10 cells after different therapies. Red JC-1 aggregate indicates mitochondria with normal membrane potential, and the green JC-1 monomer means the mitochondria with a depolarized and damaged membrane (impaired mitochondria).

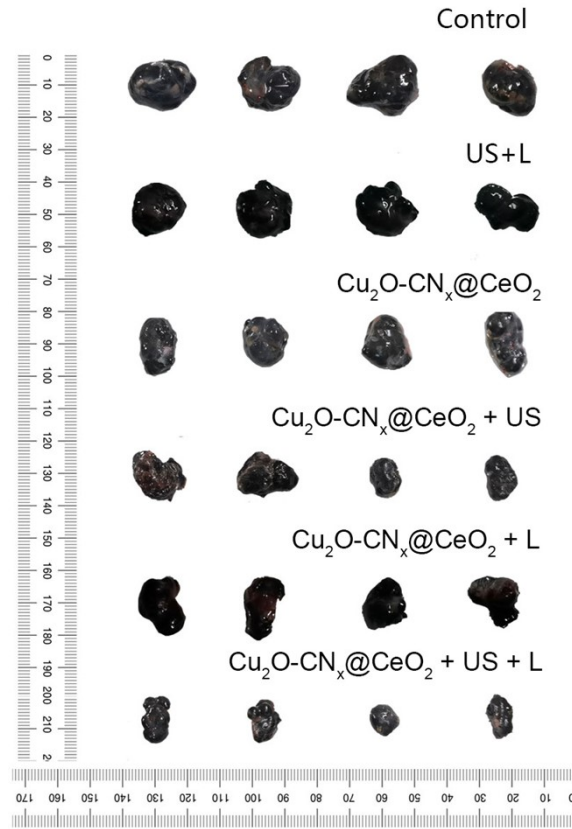


Figure S24. Tumor images of B16F10 for different treatments.

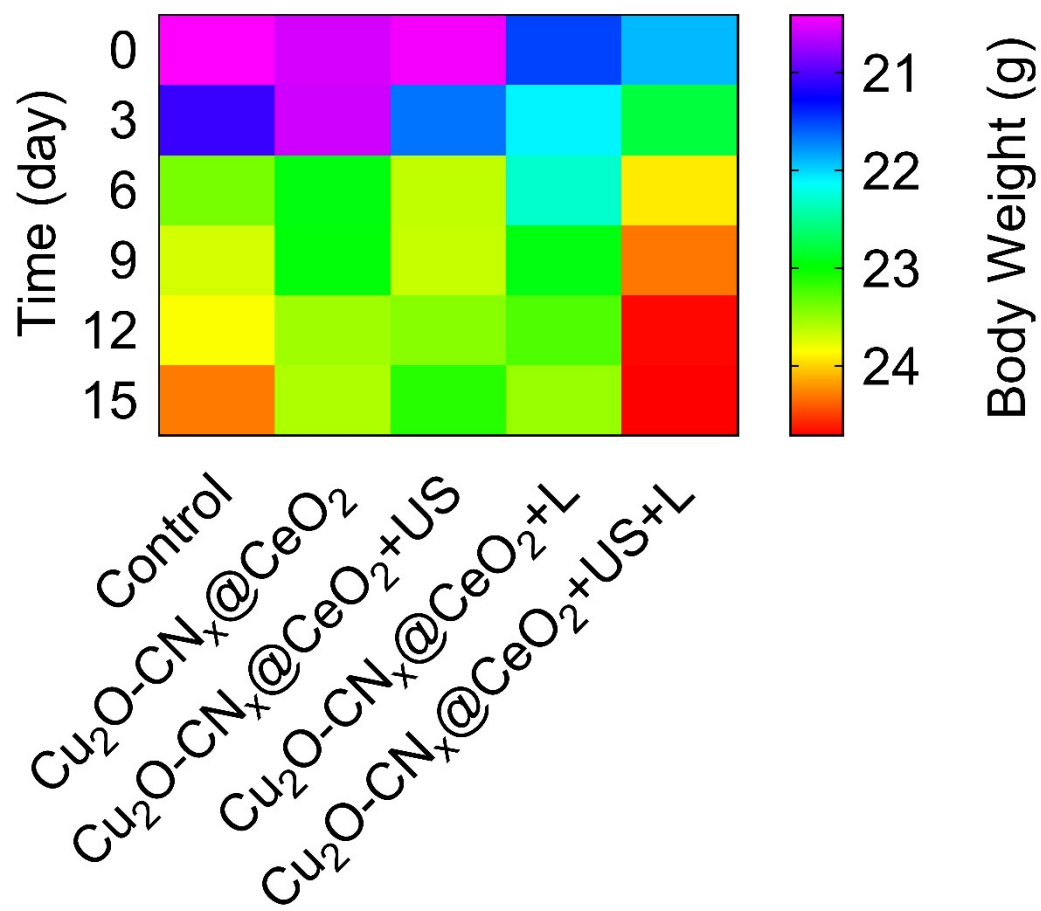


Figure S25. Changes in body weight that presented by the heat map.

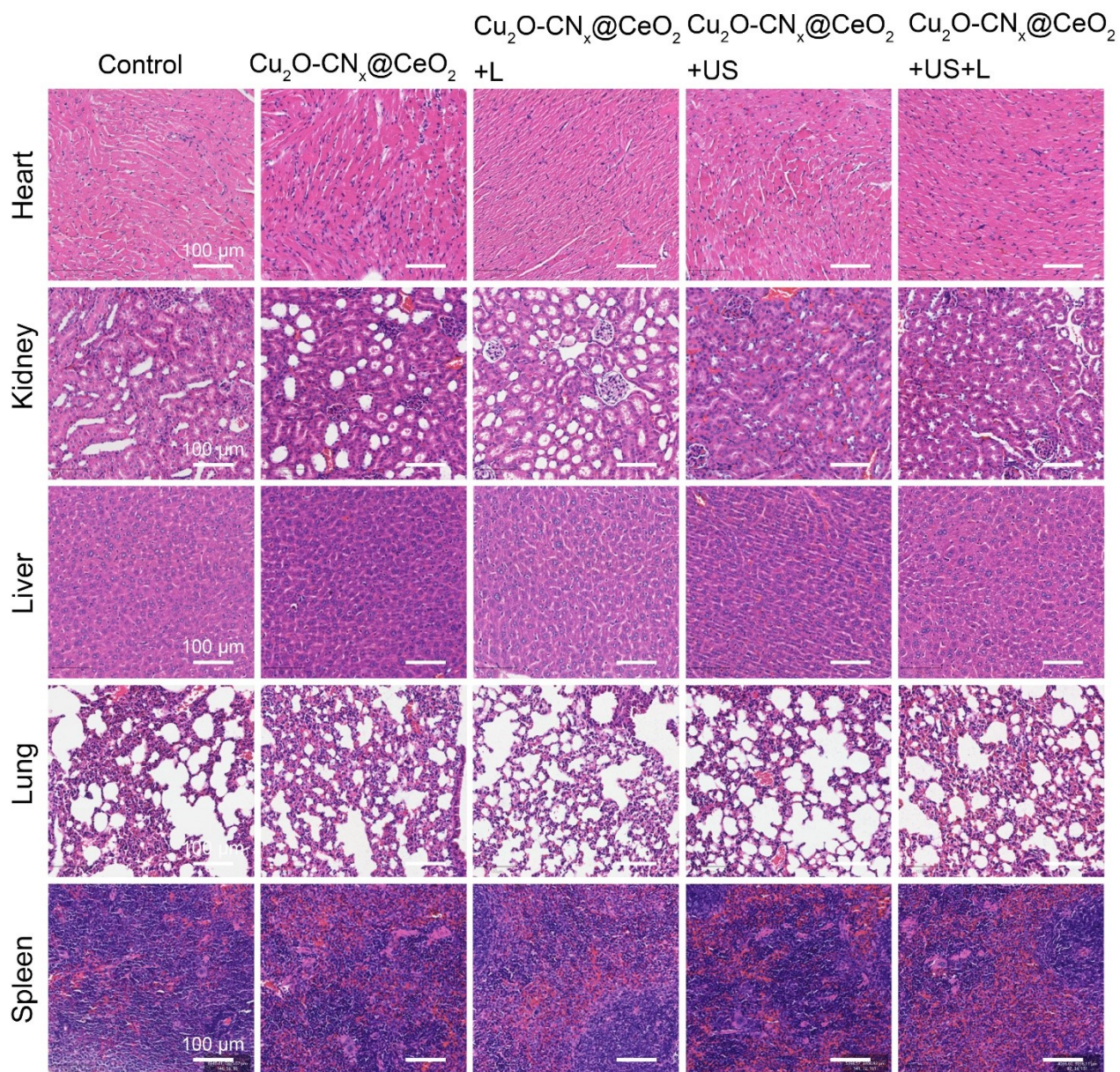


Figure S26. H&E staining of the mice's major organs (heart, liver, spleen, lung, kidney) to examine the potential accumulation of nanoagents and the histological changes after various treatments.

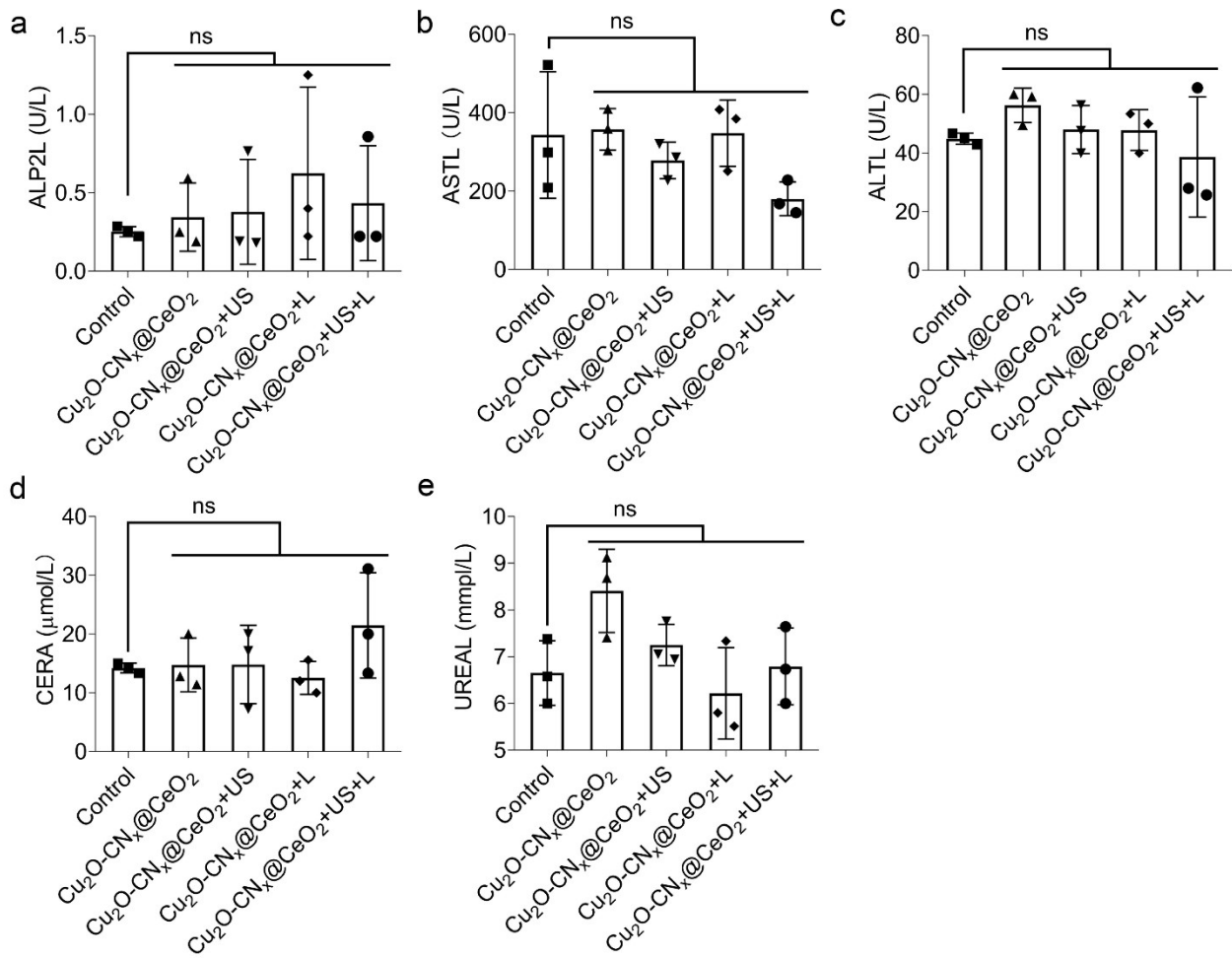


Figure S27. Blood biochemistry assays of markers (a-e) ALP2L, ALTL, ASTL, CERA, and UREAL.

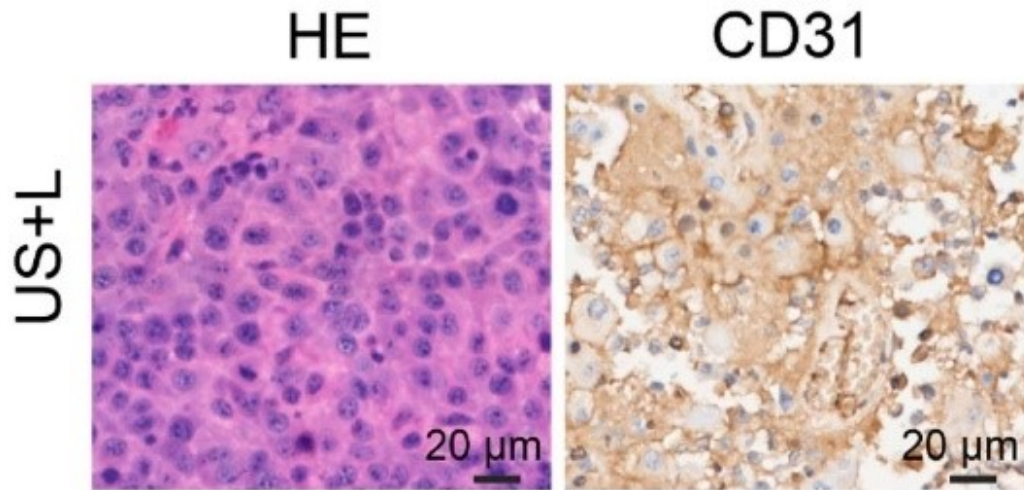


Figure S28. (a) H&E and CD31 stained images of tumor tissues and tumor blood vessels after US + L for 15 days. (b)

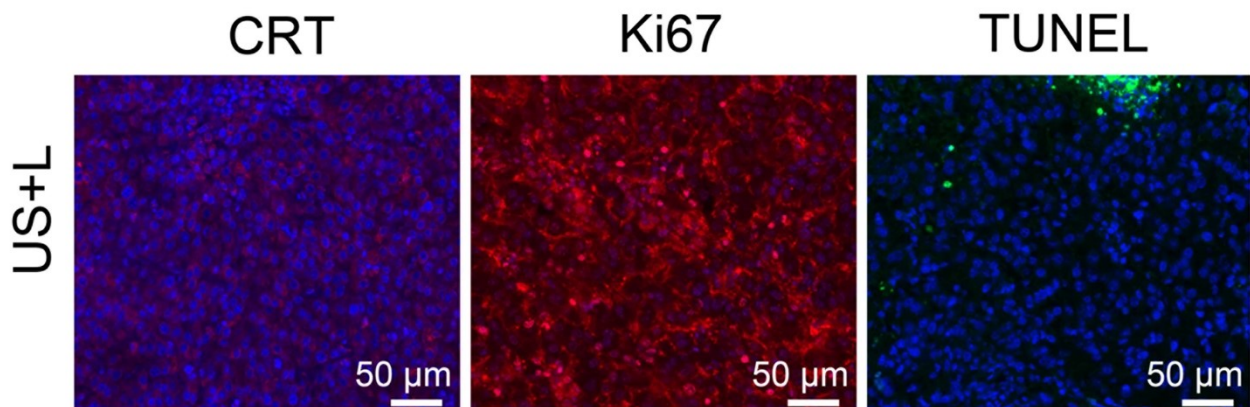


Figure S29. Images of TUNEL, Ki 67, and CRT staining of tumor sections from US + L treatment.

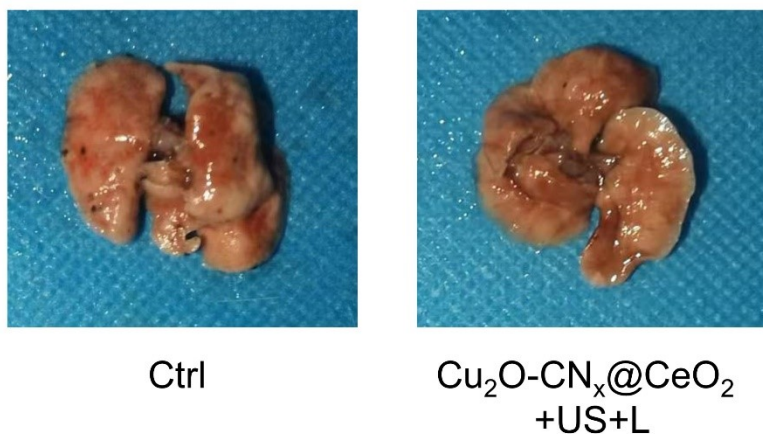


Figure S30. Images of lung metastasis before and after treatment.

Compared to the control group, the lung of $\text{Cu}_2\text{O-CN}_x@\text{CeO}_2$ + US + L treated group exhibit less metastatic melanoma

Table S1. Comparison of the POD-like catalytic kinetic constants of $\text{Cu}_2\text{O-CN}_x@\text{CeO}_2$ to H_2O_2 and other reported artificial enzymes.

Artificial enzymes	Km (mM)	Vmax ($\mu\text{M s}^{-1}$)	TON (10^{-3}s^{-1})	Ref.
$\text{Cu}_2\text{O-CN}_x@\text{CeO}_2$	3.73	0.484	14.67	This work
CoO	92.10	1.14	8.55	1
Mn_2O_3	12.53	1.01	7.979	1
Fe_2O_3	75.97	0.068	0.54	1
Fe_3O_4	41.66	0.160	1.24	1
CuO	31.18	0.280	2.24	1
Co_3O_4	41.75	0.260	2.09	1
NiO	/	0.011	0.08	1
MnO_2	/	0.064×10^{-1}	0.06	1
Mn_3O_4	/	0.013	0.10	1

Pt cube	1.00	0.018×10^{-1}	0.26	2
Ru NPs	2.21	0.580	5.858	3
Pt NCs	/	0.182	1.37	4
PtFe	217.60	0.082	2.20	5
Fe-MOF	0.13×10^{-2}	0.025	0.51	6
Cu NPs/N-C	17.98	0.086	3.32	7
Zn-N-C	40.16	0.122	2.53	7
Fe-N-C SAzymes	4.31	0.620	3.99	8
Co-N-C SAzymes	16.26	0.165	1.06	8
Zn-N-C SAzymes	6.27	0.048	0.31	8

Table S2. Comparison of nanomedicine dosage of different biocatalysts for treating the tumor cells.

Biocatalysts	Tumor type	Dosage ($\mu\text{g mL}^{-1}$)	Ref.
$\text{Cu}_2\text{O-CN}_x@\text{CeO}_2$	malignant melanoma	40	This work
PtCo	4T1	100	9
PCN-ACF-CpG@HA	H22	50	10
BMT@LA	HeLa	200	11

Reference:

1. X. Wang, X. J. Gao, L. Qin, C. Wang, L. Song, Y.-N. Zhou, G. Zhu, W. Cao, S. Lin, L. Zhou, K. Wang, H. Zhang, Z. Jin, P. Wang, X. Gao and H. Wei, *Nat. Commun.*, 2019, **10**, 704.
2. C. Ge, R. Wu, Y. Chong, G. Fang, X. Jiang, Y. Pan, C. Chen and J.-J. Yin, *Adv. Funct. Mater.*, 2018, **28**, 1801484.
3. G.-J. Cao, X. Jiang, H. Zhang, T. R. Croley and J.-J. Yin, *RSC Adv.*, 2017, **7**, 52210-52217.

4. L. Jin, Z. Meng, Y. Zhang, S. Cai, Z. Zhang, C. Li, L. Shang and Y. Shen, *ACS Appl. Mater. Interfaces*, 2017, **9**, 10027-10033.
5. S. Li, L. Shang, B. Xu, S. Wang, K. Gu, Q. Wu, Y. Sun, Q. Zhang, H. Yang, F. Zhang, L. Gu, T. Zhang and H. Liu, *Angew. Chem. Int. Ed.*, 2019, **58**, 12624-12631.
6. W. Xu, L. Jiao, H. Yan, Y. Wu, L. Chen, W. Gu, D. Du, Y. Lin and C. Zhu, *ACS Appl. Mater. Interfaces*, 2019, **11**, 22096-22101.
7. Y. Wu, J. Wu, L. Jiao, W. Xu, H. Wang, X. Wei, W. Gu, G. Ren, N. Zhang, Q. Zhang, L. Huang, L. Gu and C. Zhu, *Anal. Chem.*, 2020, **92**, 3373-3379.
8. L. Jiao, J. Wu, H. Zhong, Y. Zhang, W. Xu, Y. Wu, Y. Chen, H. Yan, Q. Zhang, W. Gu, L. Gu, S. P. Beckman, L. Huang and C. Zhu, *ACS Catal.*, 2020, **10**, 6422-6429.
9. Z. Wang, Y. Zhang, E. Ju, Z. Liu, F. Cao, Z. Chen, J. Ren and X. Qu, *Nat. Commun.*, 2018, **9**, 3334.
10. Z. Cai, F. i Xin, Z. Wei, M. Wu, X. Lin, X. Du, G. Chen, D. Zhang, Z. Zhang, X. Liu, and C. Yao, *Adv. Healthcare. Mater.* 2020, **9**, 1900996.
11. M. Wang, Z. Hou, S. Liu, S. Liang, B. Ding, Y. Zhao, M. Chang, G. Han, A. A. Al Kheraif, and J. Lin, *Small* 2021, **17**, 2005728.